PIER M

(Received 7 April 2026, Accepted 18 May 2026, Scheduled 24 May 2026)

Electromagnetic Parameter Extraction for Asymmetric Metamaterials under Oblique Incidence

Meiling Li, Zelong Fan, Dan Zeng, and Zixuan Yi*

Key Laboratory of Specialty Fiber Optics and Optical Access Networks
Shanghai Institute of Advanced Communication and Data Science, Shanghai University, Shanghai 200444, China

ABSTRACT: An improved S-parameter extraction method, based on the forward and backward propagating waves under oblique incidence on metamaterials (MMs), is proposed to accurately extract electromagnetic parameters for asymmetric uniaxial MMs in a broad frequency range. The proposed approach equivalently models asymmetric MMs as two isotropic media (distinct from the 3×3 matrix-form anisotropic medium). To validate the effectiveness of the proposed method, a low-thickness asymmetric absorptive frequency-selective surface (AFSS) and a high-thickness 7-layer absorber are designed, simulated, and analyzed.

1. INTRODUCTION

Metamaterials (MMs), as artificial electromagnetic composites, possess numerous unconventional properties, including negative permittivity and permeability, negative refractive index, and perfect absorption [1, 2]. The extraction of their electromagnetic parameters is regarded as essential for enabling applications and simplifying complex structures, leading to reduced simulation time and improved structural optimization [3]. Over recent decades, extraction techniques have been categorized into three methods: homogenization, averaging area, and scattering (S-) parameters [4–14]. The S-parameter technique is most widely applied in simulations and experiments [6–14]. In parallel, the research frontier is advancing towards real-time digital twin frameworks for electromagnetic systems [15, 16], specifically through the precise extraction of intrinsic parameters of MMs from S-parameters. The obtained high-fidelity parameters serve as critical inputs for such digital twins, bridging material characterization and system-level simulation.

Based on the interaction between MMs and incident electromagnetic waves, symmetric MMs exhibit identical reflection coefficients under forward and backward illumination, while asymmetric counterparts display distinct responses due to wave-matter interactions. Asymmetric MMs are classified into three types: inhomogeneous graded MMs [6], uniaxially anisotropic MMs [7], and biaxially anisotropic MMs [8]. Uniaxial anisotropic MMs are characterized by two equal principal components in their constitutive tensor, demonstrating a transversely isotropic electromagnetic response, whereas biaxially anisotropic MMs are defined by three distinct principal components, exhibiting fully orthotropic electromagnetic characteristics. This work develops a robust S-parameter extraction method for uniaxial anisotropic MMs. The Nicolson-Ross-Weir method and its variants are recognized as the earliest techniques for extracting electromagnetic parameters from MMs using S-parameters [9, 10] for normal incidence. Recent approaches have employed oblique-incidence S-parameters to characterize MMs [12–14], which are described by 3×3 constitutive tensors that define anisotropy and magnetoelectric coupling. In anisotropic media, the equivalent electromagnetic parameters inherently depend on both direction and frequency. At the high-frequency end of a broad frequency band, spatial dispersion begins to dominate, strongly amplifying and complicating this direction-dependent behavior. Consequently, the extracted electromagnetic parameters are confined to a narrow bandwidth, which limits their utility for broadband applications. As such, extracting broadband electromagnetic parameters for isotropic-equivalent asymmetric MMs under oblique incidence remains a significant challenge. In this letter, an improved S-parameter extraction method is proposed for the broadband electromagnetic parameter retrieval of asymmetric uniaxially MMs, based on forward and backward propagating waves under oblique incidence.

2. THEORETICAL ANALYSIS

Generally, symmetric MMs are typically treated as isotropic media under oblique incidence, whereas asymmetric ones are represented as anisotropic media. However, the anisotropic approach is only applicable within a narrow frequency band. To address this, electromagnetic parameter extraction for asymmetric MMs is performed in two stages. First, a detailed theoretical analysis of isotropic media is conducted. Subsequently, asymmetric MMs are modeled using two equivalent isotropic media.

A typical isotropic medium of thickness d immersed in vacuum is illustrated in Fig. 1 [6], with infinite extension along the x- and y-directions. TE and TM modes are denoted by their respective superscripts. θ_i, θ_t, and θ_r represent the angle of incidence, transmission, and reflection, respectively. E_i, E_t and

* Corresponding author: Zixuan Yi (yizixuan@shu.edu.cn).

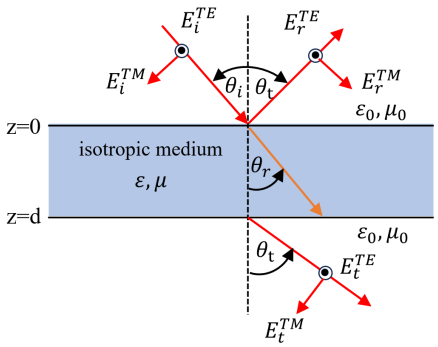

FIGURE 1. Geometry of a typical isotropic medium, illuminated by the oblique incident in both TE and TM modes.

E_r represent incident, transmitted, and reflected electric fields, respectively. ε and μ in the dielectric layer are represented as:

$$\varepsilon = \varepsilon_0\varepsilon_r = \varepsilon_0(\varepsilon_r' - j\varepsilon_r''), \quad \mu = \mu_0\mu_r = \mu_0(\mu_r' - j\mu_r'') \quad (1)$$

where ε_0 and μ_0 are the permittivity and permeability of free space; ε_r and μ_r are the relative permittivity and relative permeability of the dielectric layer; ε_r' and μ_r' are the real parts of ε_r and μ_r; ε_r'' and μ_r'' are the imaginary parts of ε_r and μ_r.

The studied asymmetric MMs exhibit distinct reflection properties, where the forward reflection S-parameters (S_{11}^{TE} and S_{11}^{TM}) differ from their backward S-parameters (S_{22}^{TE} and S_{22}^{TM}), while still adhering to reciprocity, as evidenced by the identical forward and backward transmission S-parameters ($S_{21}^{TE} = S_{12}^{TE}$, $S_{21}^{TM} = S_{12}^{TM}$). The reflection and transmission S-parameters in TE and TM modes by using sufficient boundary conditions at the air-MMs-air interfaces are derived as [12]

$$S_{11}^{TE} = \frac{\Gamma_+^{TE}\left(1-\left(T^{TE}\right)^2\right)}{1-\Gamma_+^{TE}\Gamma_-^{TE}\left(T^{TE}\right)^2},$$

$$S_{22}^{TE} = \frac{\Gamma_-^{TE}\left(1-\left(T^{TE}\right)^2\right)}{1-\Gamma_+^{TE}\Gamma_-^{TE}\left(T^{TE}\right)^2} \quad (2)$$

$$S_{21}^{TE} = S_{12}^{TE} = \frac{\left(1-\Gamma_+^{TE}\Gamma_-^{TE}\right)\left(T^{TE}\right)^2}{1-\Gamma_+^{TE}\Gamma_-^{TE}\left(T^{TE}\right)^2} \quad (3)$$

$$S_{11}^{TM} = \frac{\Gamma_+^{TM}\left(1-\left(T^{TM}\right)^2\right)}{1-\Gamma_+^{TM}\Gamma_-^{TM}\left(T^{TM}\right)^2},$$

$$S_{22}^{TM} = \frac{\Gamma_-^{TM}\left(1-\left(T^{TM}\right)^2\right)}{1-\Gamma_+^{TM}\Gamma_-^{TM}\left(T^{TM}\right)^2} \quad (4)$$

$$S_{21}^{TM} = S_{12}^{TM} = \frac{\left(1-\Gamma_+^{TM}\Gamma_-^{TM}\right)T^{TM}}{1-\Gamma_+^{TM}\Gamma_-^{TM}\left(T^{TM}\right)^2} \quad (5)$$

$$\Gamma_{+(-)}^{TE} = \frac{z_{+(-)}^{TE}-1}{z_{+(-)}^{TE}+1}, \quad \Gamma_{+(-)}^{TM} = \frac{z_{+(-)}^{TM}-1}{z_{+(-)}^{TM}+1} \quad (6)$$

$$T^{TE} = e^{-jk_0dn^{TE}}, \quad T^{TM} = e^{-jk_0dn^{TM}} \quad (7)$$

where Γ_+^{TE}, Γ_-^{TE} or Γ_+^{TM}, Γ_-^{TM} are the interfacial forward and backward reflection coefficients of the asymmetric MMs in TE or TM modes, respectively. z_+^{TE}, z_-^{TE} or z_+^{TM}, z_-^{TM} are the forward and backward normalized wave impedances of the asymmetric MMs in TE or TM modes, respectively. T^{TE} and T^{TM} represent the propagation factor in TE and TM modes. The free space wave number is given by $k_0 = \frac{f*2\pi}{c}$, where c is the speed of light in vacuum, and f is the frequency of electromagnetic waves. Additionally, n^{TE} and n^{TM} refer to the refractive indices for TE or TM modes, respectively.

It is noteworthy from (2) and (4) that the forward and backward reflection S-parameters for asymmetric MMs are different. This difference, as previously mentioned, arises from the unequal normalized wave impedance for the TE and TM modes according to (6). From an essential perspective, since the difference in forward and backward wave impedances under TE and TM modes arises from the graded impedance variation across each layer of the multilayer MMs, the asymmetric MMs described in this paper differ from bianisotropic MMs in [12–14], thereby only involving magnetic coupling and electric coupling rather than magneto-electric coupling. The derivation formula is as follows.

The first step in the proposed method is to extract z_+^{TE}, z_-^{TE}, z_+^{TM}, z_-^{TM} from S-parameters, and the magnitude of the S-parameter is less than 1. Specifically, substituting S_{11}^{TE} and S_{22}^{TE} from (2) into S_{21}^{TE} for (3); similarly substituting S_{11}^{TM} and S_{22}^{TM} from (4) into S_{21}^{TM} for (5) and by defining a set of intermediate variables $\Lambda_1, \Lambda_2, \Lambda_3, \Lambda_4$, we drive [12]

$$\Lambda_1^{TE}\left(z_+^{TE}\right)^2 + \Lambda_2^{TE}z_+^{TE} + \Lambda_4^{TE} = 0 \quad (8)$$

$$\Lambda_1^{TM}\left(z_+^{TM}\right)^2 + \Lambda_2^{TM}z_+^{TM} + \Lambda_4^{TM} = 0 \quad (9)$$

where

$$\Lambda_1^{TE} = S_{21}^{TE}S_{12}^{TE} - \left(1-S_{11}^{TE}\right)\left(1-S_{22}^{TE}\right)$$

$$\Lambda_2^{TE} = 2\left(S_{11}^{TE}-S_{22}^{TE}\right), \quad \Lambda_3^{TE} = \frac{S_{11}^{TE}-S_{22}^{TE}}{S_{11}^{TE}+S_{22}^{TE}}$$

$$\Lambda_4^{TE} = \left(1+S_{11}^{TE}\right)\left(1+S_{22}^{TE}\right) - S_{21}^{TE}S_{12}^{TE}$$

$$\Lambda_1^{TM} = S_{21}^{TM}S_{12}^{TM} - \left(1-S_{11}^{TM}\right)\left(1-S_{22}^{TM}\right)$$

$$\Lambda_2^{TM} = 2\left(S_{11}^{TM}-S_{22}^{TM}\right), \quad \Lambda_3^{TM} = \frac{S_{11}^{TM}-S_{22}^{TM}}{S_{11}^{TM}+S_{22}^{TM}}$$

$$\Lambda_4^{TM} = \left(1+S_{11}^{TM}\right)\left(1+S_{22}^{TM}\right) - S_{21}^{TM}S_{12}^{TM}$$

After z_+^{TE} and z_+^{TM} are determined as the solutions to the quadratic Equations (8) and (9), respectively, z_-^{TE} and z_-^{TM} can be obtained by combining Equations (2), (4), and (6). In this regard, z_+^{TE}, z_-^{TE}, z_+^{TM}, z_-^{TM} can be derived

$$z_+^{TE} = \left(\frac{-\Lambda_2^{TE} \pm \sqrt{\left(\Lambda_2^{TE}\right)^2 - 4\Lambda_1^{TE}\Lambda_4^{TE}}}{2\Lambda_1^{TE}}\right),$$

$$z_-^{TE} = \frac{z_+^{TE}+\Lambda_3^{TE}}{1+z_+^{TE}*\Lambda_3^{TE}} \quad (10)$$

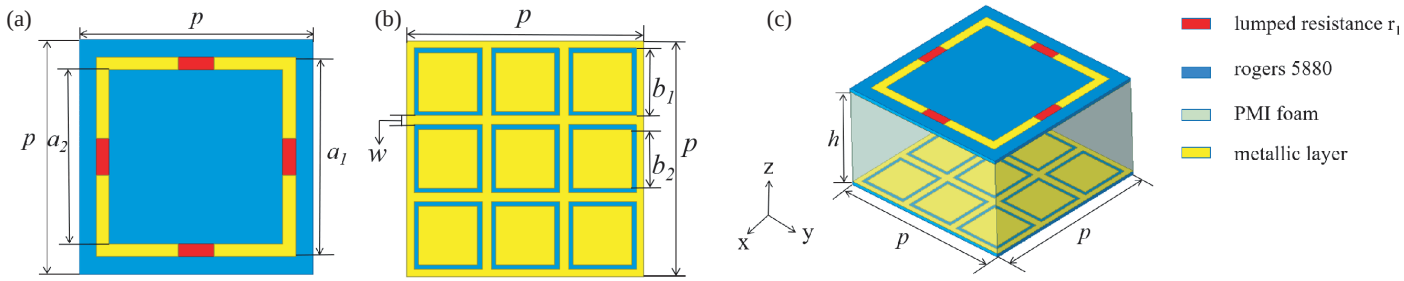

FIGURE 2. Schematic diagram of AFSS unit structure. (a) Upper-layer structure. (b) Lower-layer structure. (c) Side view of the structure. The parameter values are: $P = 12.9$, $a_1 = 11$, $a_2 = 9$, $b_1 = 3.7$, $b_2 = 3.2$, $w = 1$, $h = 7$. (Unit: mm) $r_1 = 260$ ohm.

$$z_+^{TM} = \left(\frac{-\Lambda_2^{TM} \pm \sqrt{\left(\Lambda_2^{TM}\right)^2 - 4\Lambda_1^{TM}\Lambda_4^{TM}}}{2\Lambda_1^{TM}} \right)$$

$$z_-^{TM} = \frac{z_+^{TM} + \Lambda_3^{TM}}{1 + z_+^{TM} * \Lambda_3^{TM}} \tag{11}$$

For the selection of correct sign in (8) and (9) by enforcing the passivity principle $\Re(z_+^{TE}) \geq 0$ and also $\Re(z_+^{TM}) \geq 0$, where $\Re(\cdot)$ means the real part of the complex (or real) number ".".

The second step in the proposed method is to extract refractive indices n^{TE} and n^{TM}. In this regard, T^{TE} and T^{TM} can be first extracted from S-parameters in (2), (3), (4), (5) as

$$T^{TE} = \frac{S_{11}^{TE}}{\left(1 - S_{11}^{TE}\Gamma_-^{TE}\right)} \tag{12}$$

$$T^{TM} = \frac{S_{11}^{TM}}{\left(1 - S_{11}^{TM}\Gamma_-^{TM}\right)} \tag{13}$$

where Γ_-^{TE} and Γ_-^{TM} can be obtained in (6), (10), (11). Based on the mathematical relationship provided, the refractive indices n^{TE} and n^{TM} are directly expressed in terms of the corresponding propagation factors T^{TE} and T^{TM}. Since $T^{TE} = e^{-jk_0 dn^{TE}}$ and $T^{TM} = e^{-jk_0 dn^{TM}}$, taking the natural logarithm and rearranging, the refractive indices n^{TE} and n^{TM} can be expressed as:

$$n^{TE} = \pm\frac{j\ln(T^{TE})}{k_0 d} = \pm\frac{j(\theta^{TE} + 2\pi m^{TE}) + \ln(|T^{TE}|)}{k_0 d} \tag{14}$$

$$n^{TM} = \pm\frac{j\ln(T^{TM})}{k_0 d} = \pm\frac{j(\theta^{TM} + 2\pi m^{TM}) + \ln(|T^{TM}|)}{k_0 d} \tag{15}$$

where $T^{TE} = |T^{TE}|e^{j(\theta^{TE} + 2\pi m^{TE})}$; θ^{TE} and $|T^{TE}|$ are the phases and magnitudes of the T^{TE}, respectively; $T^{TM} = |T^{TM}|e^{j(\theta^{TM} + 2\pi m^{TM})}$; θ^{TM} and $|T^{TM}|$ are the phases and magnitudes of the T^{TM}, respectively; d denotes the thickness of the asymmetric MMs. With the imaginary parts of the refractive indices satisfying $\Im(n^{TE}) < 0$, $\Im(n^{TM}) < 0$, the branch index values are given by $m^{TE} = 0, \pm1, \pm2, \ldots$ and $m^{TM} = 0, \pm1, \pm2, \ldots$, respectively. When the thickness of the MMs is less than half of the wavelength, m_1^{TE} and m_1^{TM} are assigned a value of 0. Especially for larger thicknesses of MMs, the values of m_1^{TE} and m_1^{TM} are not necessarily 0. Therefore, the phase unwrapping technique [17] has been developed to solve the ambiguity problem of the MMs with large electrical sizes.

Finally, in the case of forward oblique incident electromagnetic waves under TE and TM modes, the electromagnetic parameters μ_+^{TE}, μ_+^{TM} and ε_+^{TE}, ε_+^{TM} can be derived.

$$\mu_+^{TE} = z_+^{TE}\left(\frac{n^{TE}}{\cos\theta_i}\right), \quad \varepsilon_+^{TE} = \frac{\left(n^{TE}\right)^2 + \sin^2\theta_i}{\mu_+^{TE}} \tag{16}$$

$$\mu_+^{TM} = \frac{\left(n^{TM}\right)^2 + \sin^2\theta_i}{\varepsilon_+^{TM}}, \quad \varepsilon_+^{TM} = \frac{1}{z_+^{TM}}\frac{n^{TM}}{\cos\theta_i} \tag{17}$$

In the case of backward oblique incident electromagnetic waves under TE and TM modes, the electromagnetic parameters μ_-^{TE}, μ_-^{TM}, and ε_-^{TE}, ε_-^{TM} can be derived.

$$\mu_-^{TE} = z_-^{TE}\left(\frac{n^{TE}}{\cos\theta_i}\right), \quad \varepsilon_-^{TE} = \frac{\left(n^{TE}\right)^2 + \sin^2\theta_i}{\mu_-^{TE}} \tag{18}$$

$$\mu_-^{TM} = \frac{\left(n^{TM}\right)^2 + \sin^2\theta_i}{\varepsilon_-^{TM}}, \quad \varepsilon_-^{TM} = \frac{1}{z_-^{TM}}\frac{n^{TM}}{\cos\theta_i} \tag{19}$$

In summary, it can be obtained from (16), (17), (18), (19) that electromagnetic parameters of asymmetric MMs have been extracted by equivalently representing asymmetric uniaxial MMs as two isotropic media under oblique incidence in TE and TM modes.

3. VALIDATION AND SIMULATION

For verification purposes, an asymmetric AFSS is designed, simulated, and extracted. Comparative analyses of S-parameters are performed between the AFSS and its corresponding equivalent media models.

The geometric view of the AFSS is displayed in Fig. 2, which consists of two layers: a square ring metal with lumped resistance (positioned at the center of the square ring) and a square ring metal without lumped resistance, both printed on Rogers 5880 substrates ($\varepsilon_r = 2.2$, $\tan\delta = 0.0009$) with thickness

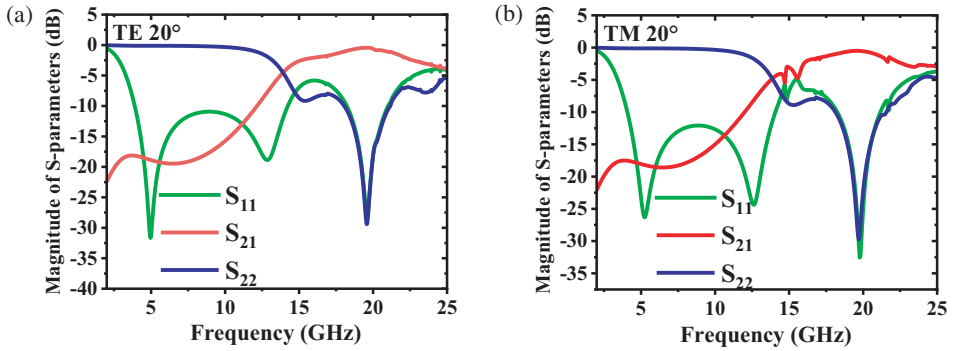

FIGURE 3. Simulated S-parameters of the AFSS for the incident angle $\theta_1 = 20°$. (a) Magnitude of S-parameters under TE mode. (b) Magnitude of S-parameters under TM mode.

$t = 0.254$ mm, paired with Polymethacrylimide (PMI) foam ($\varepsilon_r = 1.07$, $\tan\delta = 0.009$, $h = 7$ mm). The top layer features a square ring incorporating a lumped resistor at its center, forming a lossy LC resonant circuit that is responsible for electromagnetic absorption at lower frequencies. Conversely, the bottom layer consists of an array of nine unloaded square rings. This array functions as a narrowband bandpass frequency-selective surface through multiple lossless LC resonances, primarily facilitating the transmission of higher-frequency waves. Besides, the AFSS, characterized by x- and y-axis dual symmetry and periodicity, is modeled in High Frequency Structure Simulator (HFSS) via its unit cell with master and slave periodic boundary conditions and a Floquet port excitation, thus simulating an infinite array under plane wave illumination. In the simulations, tetrahedral meshing is applied (max element size: $\lambda/10$, min: 0.05 mm), and S-parameters are exported from 2 to 25 GHz at 0.05 GHz intervals, providing both magnitude (dB) and phase (degree). It should be noted that the selected angles serve merely as illustrative examples for demonstration purposes.

Within the frequency range of 2 GHz–25 GHz, the simulated S-parameters of the AFSS for the incident angle $\theta_1 = 20°$ under TE and TM modes are presented in Figs. 3(a) and (b), respectively. The S-parameters shown in Fig. 3 are imported into MATLAB (Matrix Laboratory) for the purpose of extracting the equivalent electromagnetic parameters of the AFSS. The equivalent permittivity $\varepsilon_+^{TE}, \varepsilon_-^{TE}, \varepsilon_+^{TM}, \varepsilon_-^{TM}$ and equivalent permeability $\mu_+^{TE}, \mu_-^{TE}, \mu_+^{TM}, \mu_-^{TM}$ are depicted in Figs. 4(a)–(d), which can be derived from (16), (17), (18), (19). As shown in Fig. 4, the positive and negative peaks in the equivalent permittivity and permeability at 20 GHz are attributed to a half-wavelength resonance.

A homogeneous medium with identical height to the AFSS is constructed using equivalent electromagnetic parameters derived from Figs. 4(a)–(d), simplifying the structure into a uniform material. These parameters are incorporated into the equivalent model to enable a comparison of its S-parameters between the equivalent medium and the AFSS for the TE and TM modes at $\theta_1 = 20°$. The comparison results are presented in Figs. 5(a)–(d) and Figs. 6(a)–(d), respectively. The root mean square error (RMSE) and mean absolute error (MAE) are computed across the entire frequency range to quantify global accuracy. Additionally, frequency-by-frequency acceptance thresholds are defined using the MAE as the criterion, where a deviation within 1 dB in magnitude and 10° in phase at each individual frequency point is considered acceptable. Under TE mode, the RMSEs for the magnitudes of S_{11}, S_{21}, and S_{22} over the entire 2–25 GHz band are 0.64 dB, 0.52 dB, and 0.55 dB, respectively, with corresponding MAEs of 0.25 dB, 0.21 dB, and 0.23 dB. The bandwidth specific for the magnitudes of S_{11}, S_{21}, and S_{22}, calculated as the percentage of frequency points, where the MAE is ≤ 1 dB, are 99.52%, 99.08%, and 99.21%. Under TM mode, the respective RMSEs for the magnitudes of S_{11}, S_{21}, and S_{22} are 0.76 dB, 0.67 dB, and 0.62 dB, with MAEs of 0.31 dB, 0.19 dB, and 0.33 dB, and the corresponding bandwidth-specific accuracies for the magnitudes of S_{11}, S_{21}, and S_{22} are 98.96%, 99.00%, and 99.08%. These low error values quantitatively confirm the excellent agreement visually observed in Fig. 5 and Fig. 6. Furthermore, AFSSs in [12] and [13] are modeled using a 3×3 bianisotropic matrix, which characterizes electromagnetic differences along the x-, y-, and z-directions via diagonalized permittivity and permeability tensors. This approach establishes an analytical relationship between scattering parameters and each tensor component to extract seven independent electromagnetic parameters. As shown in Fig. 7, a comparison of S_{11} between the proposed method and the method from [12] and [13] over 2–25 GHz reveals that the proposed method agrees well with the AFSS across the entire band. In contrast, the method from [12] and [13] exhibits significant deviations in S_{11}: within the 17.1–25 GHz range for the TE mode and within the 16.7–25 GHz range for the TM mode. The bandwidth-specific accuracies for the magnitude comparison of S_{11} between the equivalent medium and the AFSS under TE 20° and TM 20° incidence are 64.01% and 64.32%. It is demonstrated that the proposed method has higher translation accuracy over a wider bandwidth. These deviations are attributed to a physical mechanism: the dominance of spatial dispersion [7] at higher frequencies. For isotropic media, spatial dispersion causes the effective permittivity to evolve from a scalar function $\varepsilon_{eff}(\omega)$ to $\varepsilon_{eff}(\omega, k)$, and $\varepsilon_{eff}(\omega, k)$ can typically be expanded in a power series in the wavenumber k:

$$\varepsilon_{eff}(\omega, k) \approx \varepsilon^{(0)}(\omega) + \gamma(\omega)k^2 + \mathcal{O}\left(k^4\right) \tag{20}$$

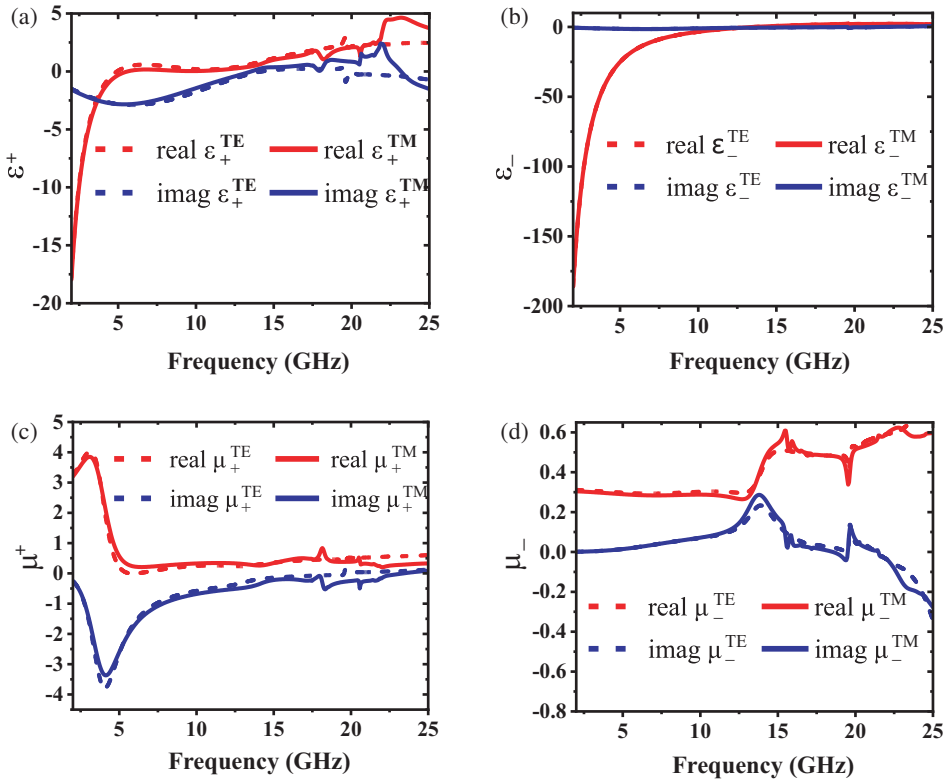

FIGURE 4. Extracted the electromagnetic parameters of the AFSS by using the S-parameters under TE and TM modes for the incident angle $\theta_1 = 20°$. Real and imag represent real and imaginary parts of the electromagnetic parameters, respectively. (a) $\varepsilon_+^{TE}, \varepsilon_+^{TM}$. (b) $\varepsilon_-^{TE}, \varepsilon_-^{TM}$. (c) μ_+^{TE}, μ_+^{TM}. (d) μ_-^{TE}, μ_-^{TM}.

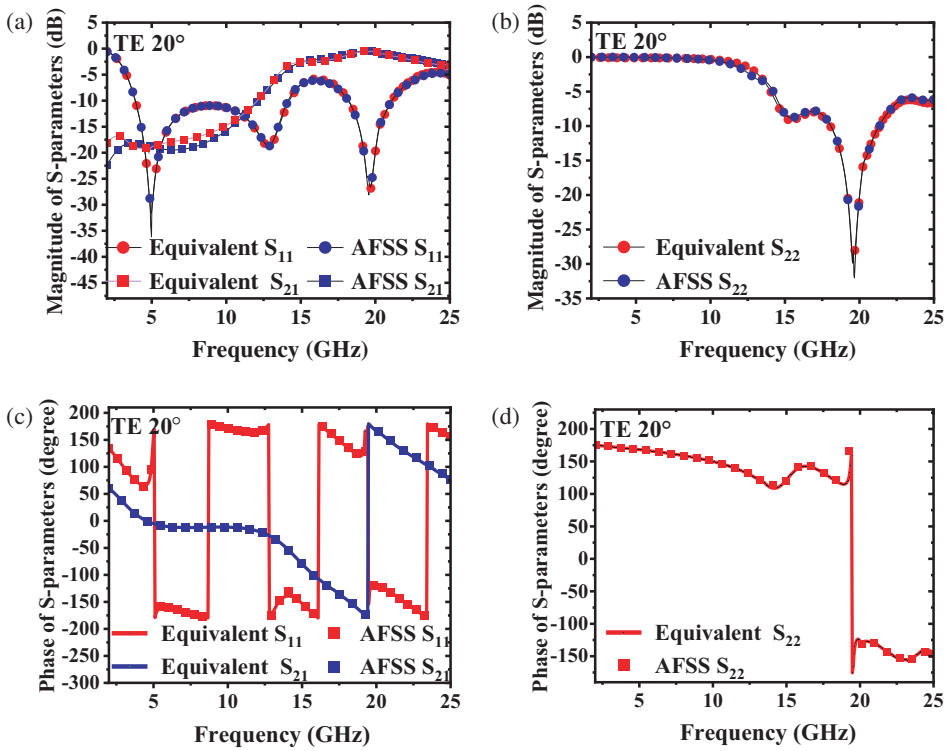

FIGURE 5. Comparisons of the S-parameters between the equivalent medium ("Equivalent") and the AFSS in TE mode for the incident angle $\theta_1 = 20°$ (HFSS simulation). (a) Magnitude of S_{11} and S_{21}. (b) Magnitude of S_{22}. (c) Phase of S_{11} and S_{21}. (d) Phase of S_{22}.

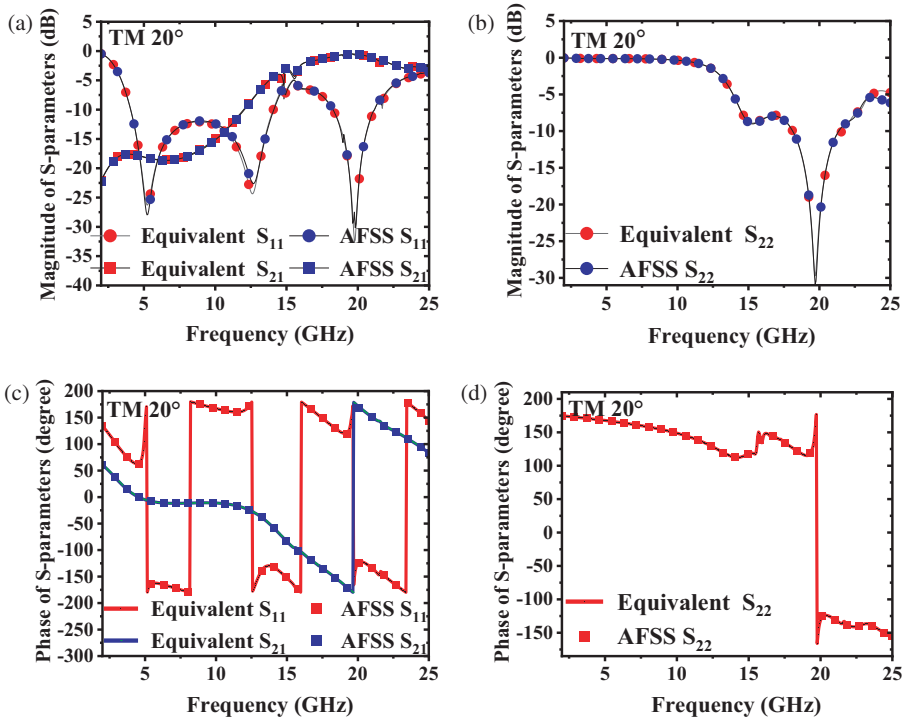

FIGURE 6. Comparisons of the S-parameters of the equivalent medium ("Equivalent") and the AFSS in TM mode for the incident angle $\theta_1 = 20°$ (HFSS simulation). (a) Magnitude of S_{11} and S_{21}. (b) Magnitude of S_{22}. (c) Phase of S_{11} and S_{21}. (d) Phase of S_{22}.

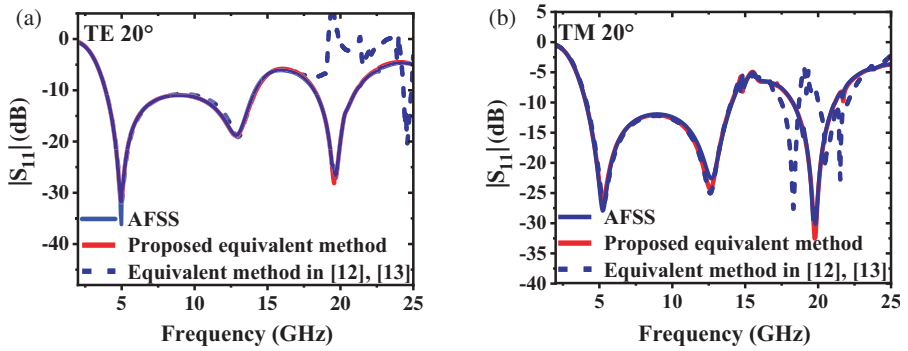

FIGURE 7. Comparisons of $|S_{11}|$ simulated by proposed equivalent method and equivalent method in [12, 13] for the incident angle $\theta_1 = 20°$ (HFSS simulation). (a) TE mode. (b) TM mode.

where $\varepsilon^{(0)}(\omega)$ represents the effective permittivity in the long-wavelength limit. The expansion coefficient $\gamma(\omega)$ is a scalar, and $\mathcal{O}(k^4)$ denotes the truncation error of higher-order spatial dispersion terms. The expression depends only on the magnitude of k and is independent of the direction of the wave vector. It implies that spatial dispersion does not alter the isotropic nature of the medium's response at high frequencies. For anisotropic media, spatial dispersion originates from the coupling of structural periodicity and directional anisotropy. The effective permittivity tensor can be expanded as:

$$\bar{\bar{\varepsilon}}_{eff}(\omega, \mathbf{k}) \approx \bar{\bar{\varepsilon}}^{(0)}(\omega) + \sum\nolimits_{i,j=x,y,z} \bar{\bar{\gamma}}^{(ij)}(\omega) k_i k_j + \mathcal{O}\left(k^4\right) \tag{21}$$

where $\bar{\bar{\varepsilon}}^{(0)}(\omega)$ is the equivalent permittivity tensor in the long-wavelength limit; $\sum_{i,j=x,y,z} \bar{\bar{\gamma}}^{(ij)}(\omega) k_i k_j$ represents the spatial dispersion correction term arising from the quadratic contribution of the wavevector; and $\mathcal{O}(k^4)$ denotes the higher-order truncation residual because $\bar{\bar{\gamma}}^{(ij)}(\omega)$ is a fourth-order tensor whose non-zero components are richer in lower-symmetry crystals, and it can further break any residual symmetry that might exist under the local approximation, making the anisotropy structure of the tensor more complex. Consequently, spatial dispersion modifies both the magnitude and symmetry of the permittivity tensor through the quadratic terms of the wave-vector components at high frequencies, causing the effective medium to exhibit stronger anisotropic behavior at finite wave vectors than in the long-wavelength limit. The accuracy of the proposed method is validated by the demonstrated consistency, as the effective suppression of the physical mechanisms is achieved under conditions of subwavelength periodicity and negligible magnetoelectric coupling.

3.1. Electromagnetic Parameters Extraction for a High-Thickness 7-Layer Asymmetric Absorber

Further, in order to validate that the proposed extraction method is also suitable for metal-film loaded dielectric MMs without the restrictions of its thickness as well as operating frequency band, electromagnetic parameters are extracted for another type of asymmetric MM, which is a high-thickness 7-layer absorber (the total height is $0.1\lambda_L$, where λ_L denotes the wavelength at the lowest frequency of the absorption band in free space). Such an absorber, shown in Fig. 8, is composed of 7-layers of PMI foam and 7-layers of resistive square patches, with resistive square patches of sheet resistance R_S printed on the PMI foam substrate [16]. Uniform surface current distribution is provided by the resistive square patches, while the PMI foam boards are lightweight and exhibit stable high-frequency characteristics. The sheet resistance values of the resistive square patches are gradually varied along the thickness direction, thereby forming a distributed-loss transmission line that enables a smooth impedance transition from free-space impedance to a low-impedance state, through which broadband impedance matching is achieved. In the low-frequency range, electromagnetic wave energy is primarily absorbed by the lower-layer high-resistance square patch, whereas in the high-frequency range, the energy is predominantly absorbed by the upper-layer low-resistance square patch. Through the synergistic effect of multi-stage distributed losses and gradient impedance, ultra-wideband absorption performance is realized over the 1–40 GHz range. Moreover, the 7-layer absorber structure is designed with biaxial symmetry in a periodic configuration. While the proposed extraction method is applicable to arbitrary incidence angles, two representative cases ($\theta_2 = 3°$ and $\theta_2 = 60°$) are simulated in HFSS for demonstration purposes.

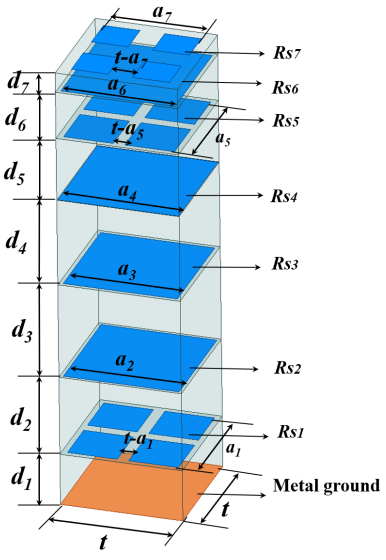

FIGURE 8. Geometrical details of an ultra-wideband absorber structure with 7-layers of resistive films and 7-layers of PMI foam. The parameter values are: $t = 15$, $d_1 = 6.5$, $d_2 = 10$, $d_3 = 12$, $d_4 = 11$, $d_5 = 10$, $d_6 = 8$, $d_7 = 6$, $a_1 = 13.6$, $a_2 = 14.2$, $a_3 = 14$, $a_4 = 14.8$, $a_5 = 13.6$, $a_6 = 14$, $a_7 = 12$. (unit: mm) $R_{S1} = 110$, $R_{S2} = 382$, $R_{S3} = 382O$, $R_{S4} = 842$, $R_{S5} = 842$, $R_{S6} = 842$, $R_{S7} = 110$. (unit: Ohm/sq).

Due to the presence of a metal ground in the absorber, the absorber cannot be penetrated by electromagnetic waves, resulting in S_{22} being equal to 1. From (10), it can be seen that when a metal ground plane is present, the wave impedance becomes zero, rendering the formula meaningless. Therefore, in the subsequent process of extracting electromagnetic parameters, the metal ground will be removed, and the absorber will be treated as an asymmetric structure overall. Within the frequency range of 1 GHz–40 GHz, the simulated S-parameters of the 7-layer absorber at a 60° oblique incidence angle under TE and TM modes are presented in Figs. 9(a) and (b), respectively.

The original phase for the refractive index phase under TM mode is shown in Fig. 10(a), where the phase oscillates back and forth between $-180°$ and $+180°$. The reason is that the thickness of the absorber is much larger than the wavelength of electromagnetic waves, causing the material boundaries to be close to each other. If $d < \lambda/2$ (λ is the wavelength corresponding to the maximum operating frequency of MMs), phase ambiguity can be avoided, while if $d > \lambda/2$, phase ambiguity will occur, which will be solved by the K-K relation and phase compensation method [18]. Therefore, the modified refractive index phase is displayed in Fig. 10(b), which is represented as a straight line.

To derive the equivalent electromagnetic parameters of the absorber, the S-parameters illustrated in Fig. 9 are imported into MATLAB. The electromagnetic parameters, after being modified for the refractive index phase, are presented in Fig. 10. The equivalent permittivity $\varepsilon_+^{TE}, \varepsilon_-^{TE}, \varepsilon_+^{TM}, \varepsilon_-^{TM}$ and equivalent permeability $\mu_+^{TE}, \mu_-^{TE}, \mu_+^{TM}, \mu_-^{TM}$ are depicted in Figs. 11(a)–(d), which can be derived from (16), (17), (18), (19). Subsequently, the equivalent electromagnetic parameters in Fig. 11 are integrated into an equivalent medium of the same height as the 7-layer absorber to enable a comparative analysis of the S-parameters between the simulated 7-layer absorber and its equivalent medium. The S-parameters of the equivalent medium and 7-layer absorber without metal ground under TE and TM modes are presented in Figs. 12(a)–(d) when $\theta_2 = 30°$, respectively. Under TE mode, the RMSE for the magnitudes of S_{11} and S_{22} over the entire 1–40 GHz band are 0.32 dB and 0.56 dB, respectively, with the corresponding MAEs of 0.25 dB and 0.24 dB. Under TM mode, the RMSEs for S_{11} and S_{22} are 0.43 dB and 0.55 dB, respectively, with the corresponding MAEs of 0.21 dB and 0.16 dB. The bandwidth-specific accuracies, defined as the percentage of frequency points, where the MAE is $\leq$ 1 dB, are 98.95% for S_{11} and 99.9% for S_{22} under TE mode, and 99.26% for S_{11} and 98.21% for S_{22} under TM mode. Meanwhile, the S-parameters of the equivalent medium and 7-layer absorber without metal ground under TE and TM modes are presented in Figs. 13(a)–(d) when $\theta_2 = 30°$, respectively. Under TE mode, the RMSE and MAE for the magnitude of S_{11} are 0.62 dB and 0.27 dB, respectively, with a bandwidth-specific accuracy of 97.98% where the MAE is $\leq$ 1 dB. Under TM mode, the corresponding RMSE and MAE for the magnitude of S_{11} are 0.56 dB and 0.22 dB, with a bandwidth-specific accuracy of 98.44%. To demonstrate the applicability of the proposed method for the electromagnetic parameter extraction of MMs under varying oblique incidence angles, the S-parameters of the equivalent medium and 7-layer

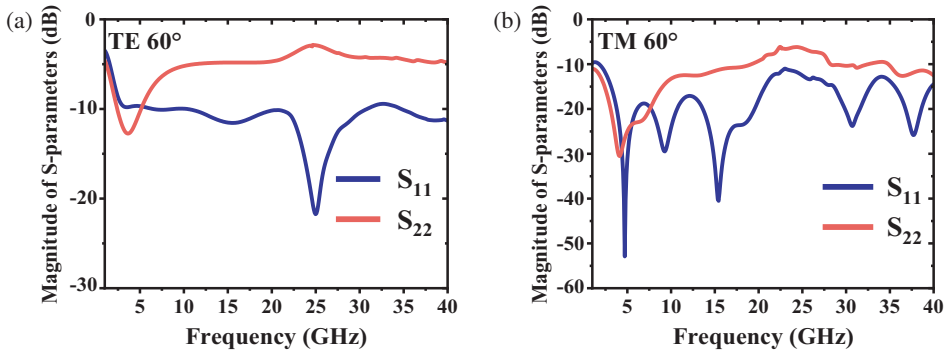

FIGURE 9. Simulated S-parameters of 7-layer absorber for the incident angle $\theta_2 = 60°$. (a) Magnitude of S-parameters under TE mode. (b) Magnitude of S-parameters under TM mode.

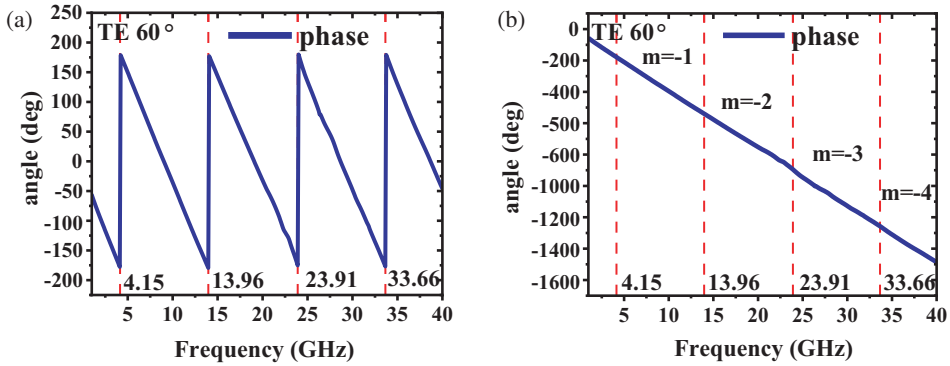

FIGURE 10. Extracted refractive index phase of the 7-layer absorber under TM mode for the incident angle $\theta_2 = 60°$. (a) Original phase of n^{TM}. (b) Modified phase of n^{TM}.

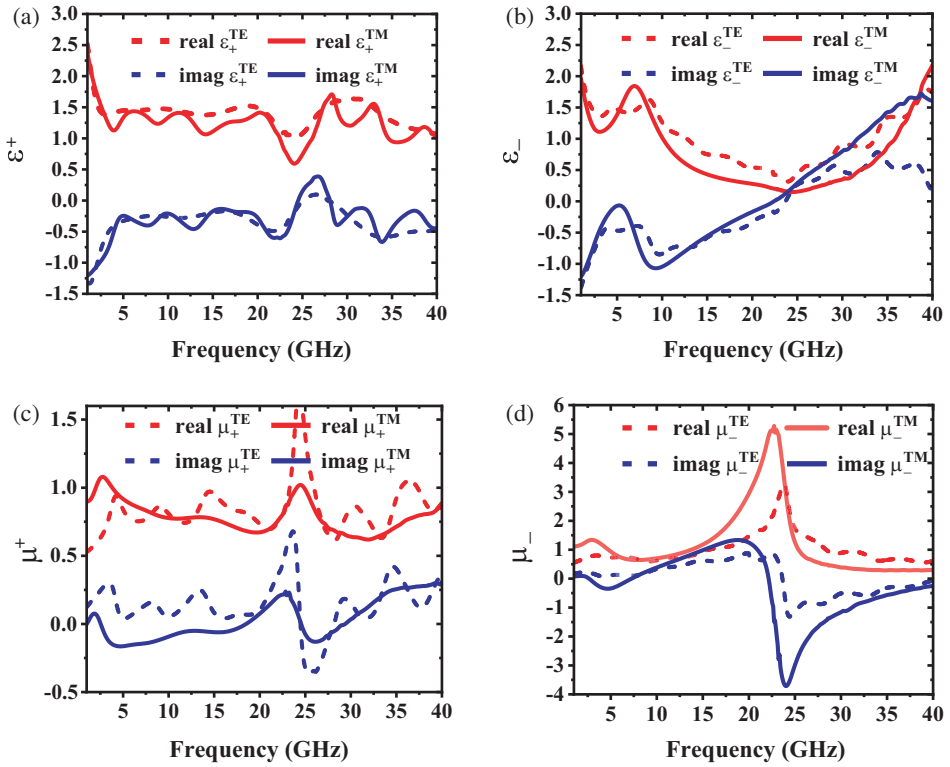

FIGURE 11. Extracted electromagnetic parameters of 7-layer absorber by using the S-parameters under TE and TM modes for the incident angle $\theta_2 = 60°$. (a) $\varepsilon_+^{TE}, \varepsilon_+^{TM}$. (b) $\varepsilon_-^{TE}, \varepsilon_-^{TM}$. (c) μ_+^{TE}, μ_+^{TM}. (d) μ_-^{TE}, μ_-^{TM}.

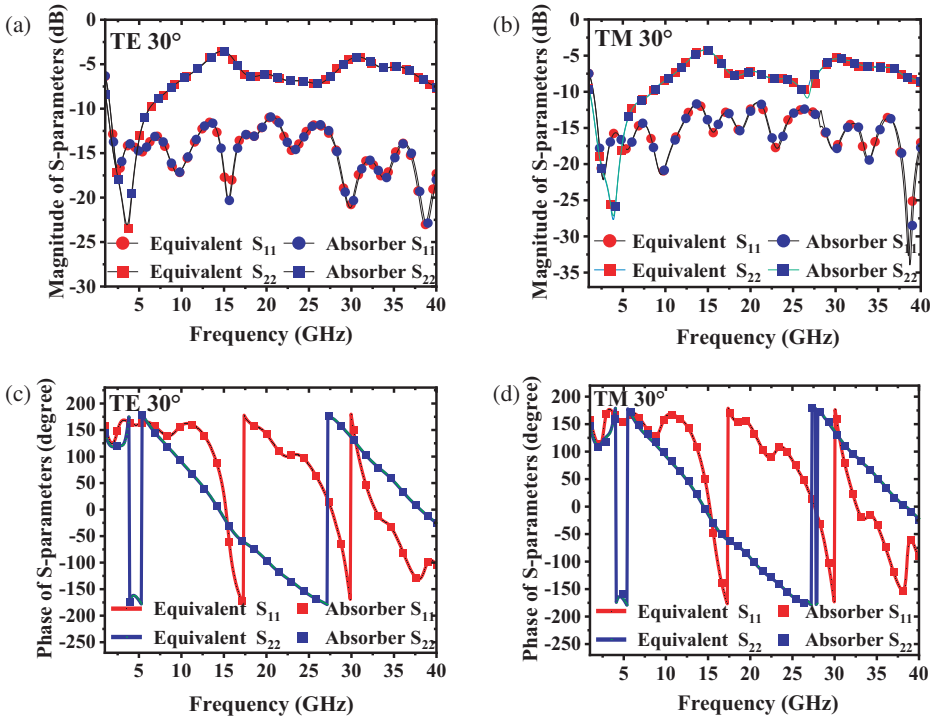

FIGURE 12. Comparisons of the S-parameters of the equivalent medium ("Equivalent") and a 7-layer absorber without a metal ground for the incident angle $\theta_2 = 30°$ (HFSS simulation). (a) Magnitude of S_{11} and S_{22} under TE mode. (b) Magnitude of S_{11} and S_{22} under TM mode. (c) Phase of S_{11} andS_{22} under TE mode. (d) Phase of S_{11} and S_{22} under TM mode.

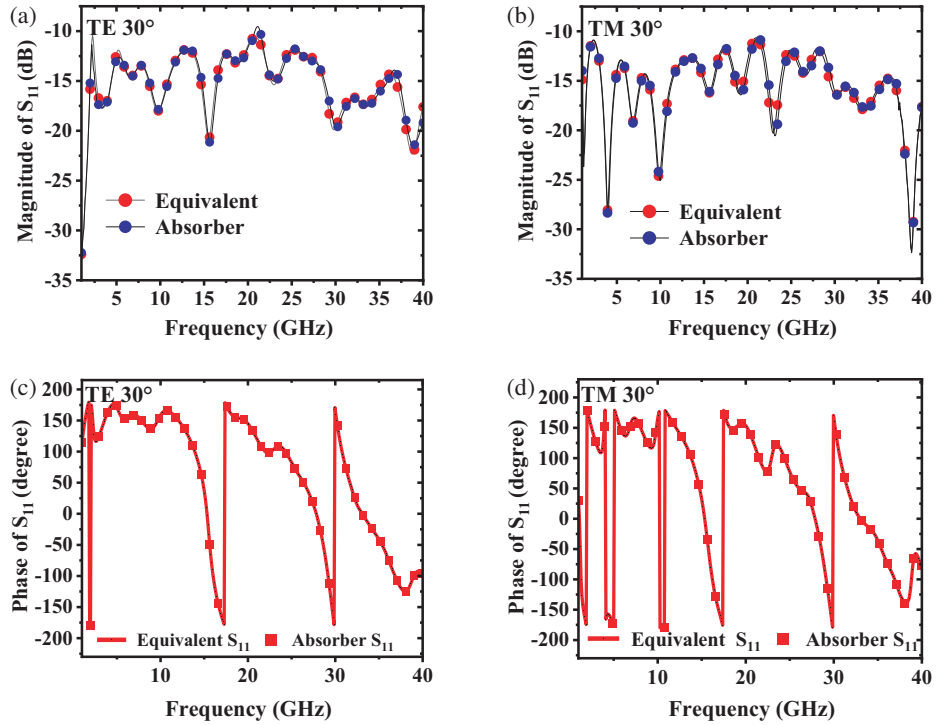

FIGURE 13. Comparisons of the S-parameters of the equivalent medium ("Equivalent") and a 7-layer absorber with a metal ground for the incident angle $\theta_2 = 30°$ (HFSS simulation). (a) Magnitude of S_{11} under TE mode. (b) Magnitude of S_{11} under TM mode. (c) Phase of S_{11} under TE mode. (d) Phase of S_{11} under TM mode.

absorber without metal ground under TE and TM modes are presented in Figs. 14(a)–(d) when $\theta_2 = 60°$, respectively. Under TE mode, the RMSE for the magnitudes of S_{11} and S_{22} are 0.44 dB and 0.53 dB, respectively, with teh corresponding MAEs of 0.22 dB and 0.28 dB. Under TM mode, the RMSEs for S_{11} and S_{22} are 0.42 dB and 0.66 dB, respectively, with the

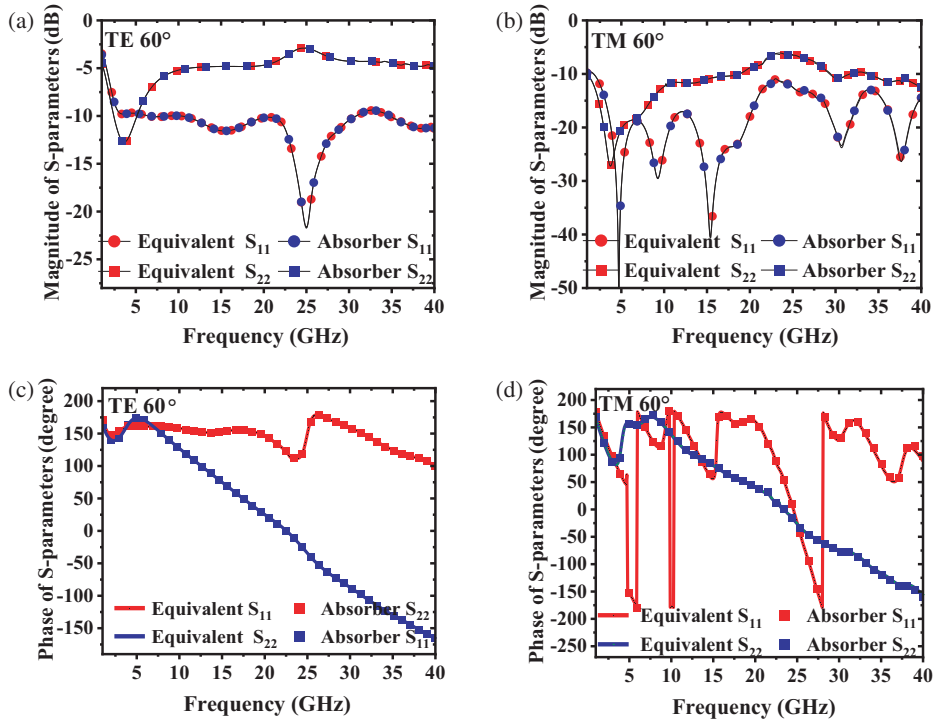

FIGURE 14. Comparisons of the S-parameters of the equivalent medium ("Equivalent") and a 7-layer absorber without a metal ground for the incident angle $\theta_2 = 60°$ (HFSS simulation). (a) Magnitude of S_{11} and S_{22} under TE mode. (b) Magnitude of S_{11} and S_{22} under TM mode. (c) Phase of S_{11} and S_{22} under TE mode. (d) Phase of S_{11} and S_{22} under TM mode.

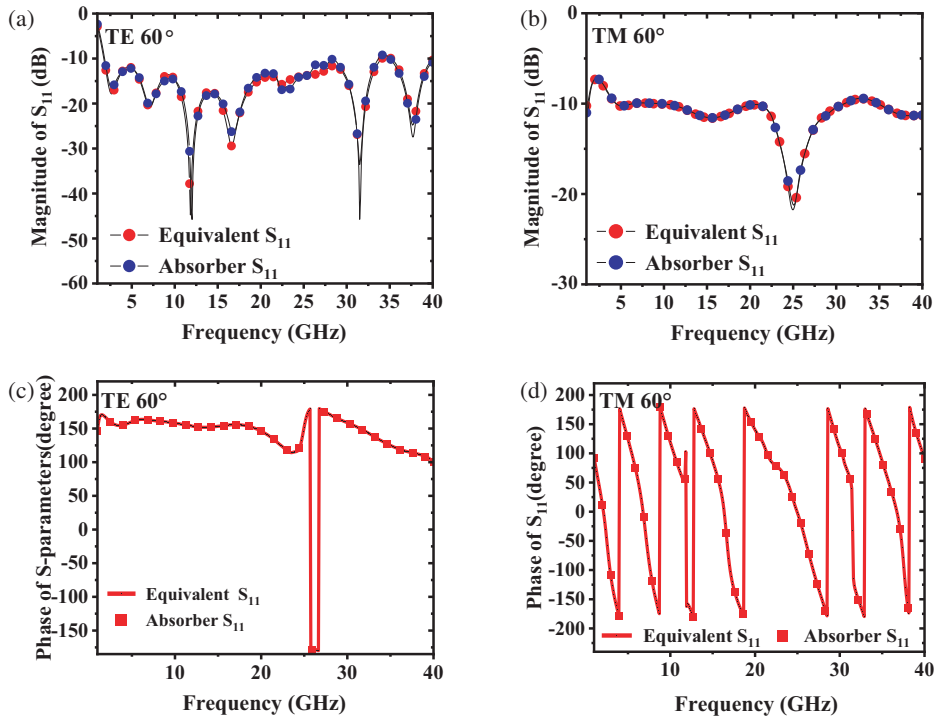

FIGURE 15. Comparisons of the S-parameters of the equivalent medium ("Equivalent") and a 7-layer absorber with a metal ground for the incident angle $\theta_2 = 60°$ (HFSS simulation). (a) Magnitude of S_{11} under TE mode. (b) Magnitude of S_{11} under TM mode. (c) Phase of S_{11} under TE mode. (d) Phase of S_{11} under TM mode.

corresponding MAEs of 0.23 dB and 0.22 dB. The bandwidth-specific accuracies are 98.92% for S_{11} and 99.51% for S_{22} under TE mode, and 98.94% for S_{11} and 99.21% for S_{22} under TM mode. Meanwhile, the S-parameters of the equivalent medium and 7-layer absorber without metal ground under TE and TM modes are presented in Figs. 15(a)–(d) when $\theta_2 = 60°$, respectively. Under TE mode, the RMSE and MAE for the magnitude of S_{11} are 0.52 dB and 0.23 dB, respectively, with

a bandwidth-specific accuracy of 98.56%. Under TM mode, the corresponding RMSE and MAE for the magnitude of S_{11} are 0.48 dB and 0.19 dB, with a bandwidth-specific accuracy of 99.08%. The S-parameters derived from the equivalent method show fundamental agreement with those of the original structure across the 1–40 GHz frequency range, demonstrating the method's capability to extend electromagnetic parameter extraction to broader bandwidths, even for high-thickness MMs.

4. CONCLUSION

The article proposes an S-parameter technique for extracting the equivalent electric permittivity and magnetic permeability from both symmetric and asymmetric MMs by analyzing forward and backward propagating waves under oblique incidence. The innovation of this extraction method lies in the introduction of two isotropic media (distinct from the 3×3 matrix-form anisotropic medium), which effectively suppresses spatial dispersion effects on the extracted electromagnetic parameters and expands the frequency range for parameter extraction, provided that no half-wavelength resonance points occur within the operating band. Two types of MMs, featuring low-thickness and high-thickness configurations, are implemented to validate and evaluate the accuracy of the proposed method. Compared to similar methods reported in the literature, the proposed method demonstrates higher accuracy. This method provides a new approach to addressing the challenges of simulating large-scale MMs over a broad frequency band. In summary, an effective method is provided by this research for extracting electromagnetic parameters of MMs under oblique incidence, thus breaking the limitation of the thickness of MMs and solving the problem of inaccurate extraction of electromagnetic parameters for asymmetric MMs within a broad frequency range, which has been verified for accuracy and universality in practical applications.

ACKNOWLEDGEMENT

This work was supported by the National Natural Science Foundation of China under Grant No. 52207214.

REFERENCES

[1] Chau, Y.-F. C., "Advances in fano resonance-based metal–insulator–metal plasmonic sensors: Mechanisms, applications, and future perspectives," *Optics & Laser Technology*, Vol. 194, 114487, 2026.

[2] Wang, C., W. R. Sweeney, A. D. Stone, and L. Yang, "Coherent perfect absorption at an exceptional point," *Science*, Vol. 373, No. 6560, 1261–1265, Sep. 2021.

[3] Weir, W. B., "Automatic measurement of complex dielectric constant and permeability at microwave frequencies," *Proceedings of the IEEE*, Vol. 62, No. 1, 33–36, Jan. 1974.

[4] Yang, Z., X.-W. Yuan, X.-W. Huang, M.-L. Yang, and X.-Q. Sheng, "Resistive sheet boundary condition-based nonconformal domain decomposition FE-BI-MLFMA for electromagnetic scattering from inhomogeneous objects with honeycomb structures," *IEEE Transactions on Antennas and Propagation*, Vol. 70, No. 10, 9483–9496, Oct. 2022.

[5] Barroso, J. J., A. Tomaz, and U. C. Hasar, "Refractive properties of wire-grid metamaterials," *Journal of Electromagnetic Waves and Applications*, Vol. 28, No. 3, 389–398, 2014.

[6] Kim, D., C. Y. Park, C.-H. Lee, and Y. J. Yoon, "Four-arm log-periodic toothed antenna with hybrid reflector composed of inhomogeneous metamatarial elements for electronic support measures," *IEEE Access*, Vol. 11, 104 735–104 744, 2023.

[7] Mota, A. F., A. Martins, J. Weiner, F. L. Teixeira, and B.-H. V. Borges, "Constitutive parameter retrieval for uniaxial metamaterials with spatial dispersion," *Physical Review B*, Vol. 94, No. 11, 115410, 2016.

[8] Hasar, U. C. and M. Bute, "Method for retrieval of electromagnetic properties of inhomogeneous reciprocal chiral metamaterials," *IEEE Transactions on Antennas and Propagation*, Vol. 68, No. 7, 5714–5717, Jul. 2020.

[9] Hasar, U. C., "Thickness-invariant complex permittivity retrieval from calibration-independent measurements," *IEEE Microwave and Wireless Components Letters*, Vol. 27, No. 2, 201–203, Feb. 2017.

[10] Shi, Y., T. Hao, L. Li, and C.-H. Liang, "An improved NRW method to extract electromagnetic parameters of metamaterials," *Microwave and Optical Technology Letters*, Vol. 58, No. 3, 647–652, Mar. 2016.

[11] Hasar, U. C. and H. Ozturk, "Feasible extraction method for permittivity determination of reflection-asymmetric structures," *IEEE Transactions on Microwave Theory and Techniques*, Vol. 73, No. 2, 1009–1016, Feb. 2025.

[12] Ozturk, G., U. C. Hasar, M. Bute, and M. Ertugrul, "Determination of constitutive parameters of strong-coupled bianisotropic metamaterials using oblique incidence scattering parameters," *IEEE Transactions on Antennas and Propagation*, Vol. 69, No. 2, 918–927, Feb. 2021.

[13] Cohen, D. and R. Shavit, "Bi-anisotropic metamaterials effective constitutive parameters extraction using oblique incidence S-parameters method," *IEEE Transactions on Antennas and Propagation*, Vol. 63, No. 5, 2071–2078, May 2015.

[14] Zhong, L., S. Sun, P.-Y. Chen, and J. Hu, "An efficient method to extract the effective permittivity of the honeycomb composite," in *2023 International Applied Computational Electromagnetics Society Symposium (ACES-China)*, 1–2, Hangzhou, China, 2023.

[15] Pandey, R. and N. Kumar, "State-space model-based digital twin with real-time parameter optimization using MDA-EFO for grid-connected PV inverter systems," *IEEE Transactions on Circuits and Systems I: Regular Papers*, Vol. 73, No. 5, 3739–3749, May 2026.

[16] Pandey, R. and N. Kumar, "A digital twin-based stability monitoring and parameter estimation framework for three-phase grid-connected photovoltaic inverters," *IEEE Transactions on Power Electronics*, Vol. 41, No. 4, 6304–6313, Apr. 2026.

[17] Hasar, U. C., A. Muratoglu, M. Bute, J. J. Barroso, and M. Ertugrul, "Effective constitutive parameters retrieval method for bianisotropic metamaterials using waveguide measurements," *IEEE Transactions on Microwave Theory and Techniques*, Vol. 65, No. 5, 1488–1497, May 2017.

[18] Li, M., C. Zhang, X.-X. Yang, D. Zeng, and Z. Yi, "An ultrawideband and wide-angle absorber based on mushroom-type high impedance surface," *IEEE Antennas and Wireless Propagation Letters*, Vol. 23, No. 12, 4368–4372, Dec. 2024.